

Multiple structural forms of a vacancy in silicon as evidenced by vacancy profiles produced by rapid thermal annealing

Vladimir Voronkov* and Robert Falster**

SunEdison, via Nazionale 59, Merano 39012, Italy

Received 8 April 2014, revised 30 April 2014, accepted 30 April 2014

Published online 10 September 2014

Keywords diffusion, reconstruction, silicon, vacancy

* Corresponding author: e-mail vvoronkov@sunedison.it, Phone: +39 0473 333 308, Fax: +39 0473 333 270

** e-mail rfalster@sunedison.com, Phone: +44 20 7704 9845, Fax: +39 0473 333 270

Vacancy depth profiles installed by rapid thermal annealing can be monitored either by Pt diffusion or through vacancy-assisted oxygen precipitation. The features of these profiles clearly show that the vacancy species manifested in these experiments is a “slow vacancy”, V_s . The evolution of V_s depth profiles is controlled by an exchange with another (mobile) kind of vacancy that is likely to be a “Watkins vacancy”, V_w , first observed at cryogenic temperatures. At low T the conversion of V_s into V_w is slow and practically irreversible. At higher T the

two species coexist in an equilibrium ratio and diffuse as one entity with an averaged diffusivity. This model provides a good fit to the RTA-installed depth profiles of V_s . The total vacancy community includes, beside V_s and V_w , also a fast vacancy V_f that is responsible for the vacancy contribution into self-diffusion at high T . In RTA experiments, the V_f species seems to be completely annihilated by self-interstitials which leaves only two other vacancy species, V_s and V_w .

© 2014 WILEY-VCH Verlag GmbH & Co. KGaA, Weinheim

1 Introduction Silicon vacancies play a key role in many phenomena such as impurity diffusion [1], production of point defects by irradiation [2–4] and formation of grown-in microdefects [5]. In spite of many efforts, the vacancy properties are still not well defined. It appears [6] that the vacancy problem is even more complicated than it was thought in the past: the vacancy in silicon exists not just as a single species, with a definite temperature-dependent diffusivity. It is rather represented by several structural forms, strongly differing in the diffusivity. The available data on the apparent vacancy diffusivity [6, 7] are collected in Fig. 1. The upper solid line is the diffusivity found at cryogenic temperatures by Watkins [4] and extrapolated to high T . The diffusivity deduced from the properties of grown-in voids [5], referring to a typical void formation temperature of 1100 °C, is shown by a bar confined by rhombic symbols. This value is similar to the Watkins diffusivity. However, there are other data showing a much slower vacancy diffusion. The diffusivity deduced [6] from the enhanced self-diffusion under hot proton irradiation [8] is lower by three orders of magnitude (circles in Fig. 1). The diffusivity deduced [6] by the data on rapid thermal

annealing (RTA) at about 1260 °C is marked by a bar confined by squares. The diffusivity estimated from the evolution of the RTA-induced vacancy profiles by subsequent annealing at 975 °C [7] is marked by a downward arrow. The values shown in Fig. 1 seemingly form two distinct groups. The first group corresponds to a high diffusivity with a weak dependence on T . The second group corresponds to a much lower diffusivity, with a strong apparent dependence on T . The data of Fig. 1 can be explained only if there are at least two kinds of vacancy differing in diffusivity. In the present work, we show that the RTA-induced vacancy depth profiles can be quantitatively fitted within a concept of two co-existing vacancy species.

The effect of RTA to install a depth profile of vacancy species, $C_v(z)$, is long known [9, 10], and this approach provides the most straightforward way to study the vacancy properties. The vacancy profile can be monitored directly [9, 10] by in-diffusion of metals with an appreciable substitutional component, like Pt, which leads to replacement of the vacancy species with substitutional metal atoms measurable by DLTS. Another approach, indirect but simple and efficient, is to trace the depth profile $N(z)$ of

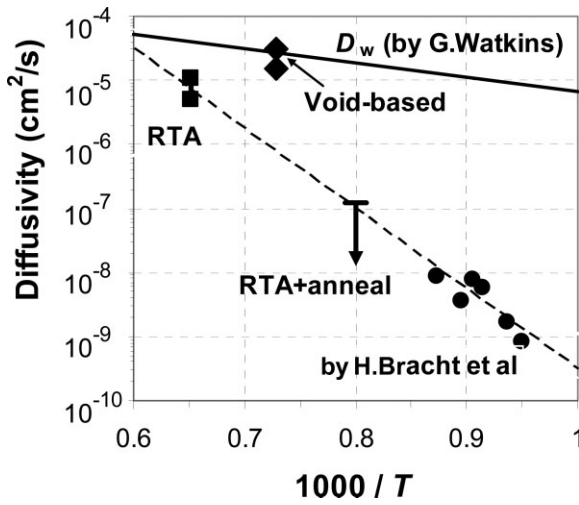


Figure 1 Data on the vacancy diffusivity deduced from different experiments (described in the text).

oxide precipitates produced by a proper annealing of wafers with RTA-installed vacancy profiles. It was found [10] that N is a power function of C_V with an exponent close to three. The reported profiles, both $C_V(z)$ and $N(z)$, have peculiar features indicating a transformation between two different kinds of vacancy.

2 Depth profiles of vacancy species monitored by Pt diffusion If the RTA ambient is Ar, the Pt-monitored vacancy depth profile [7, 9, 10] looks like an almost flat middle portion surrounded by narrow near-surface depleted regions (roughly 60 μm wide); an example is shown in Fig. 2 by the curve 1. The near-surface depletion is due to vacancy out-diffusion in the course of fast cooling

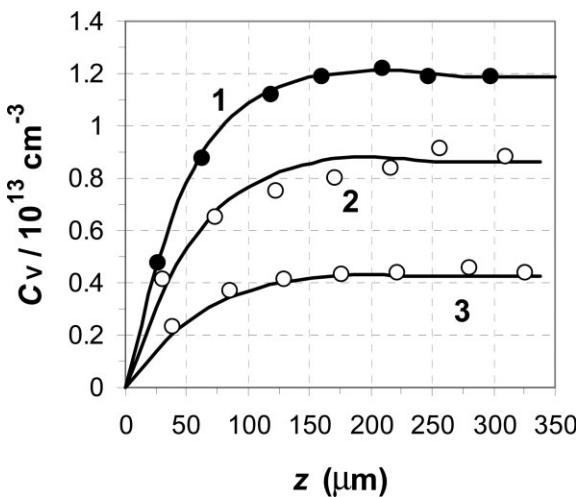


Figure 2 Depth profiles of Pt-monitored vacancy concentration [7]. The curve 1 (filled circles) is right after RTA (1240 °C/20 s in Ar ambient, cooling at 70 K/s). The curves 2 and 3 are after subsequent anneal at 975 °C for 18 and 58 s, respectively.

that follows a short holding of a sample at T_{RTA} . The time scale of cooling is several seconds, and the resulting estimate for the vacancy diffusivity at T_{RTA} is roughly $10^{-5} \text{ cm}^2/\text{s}$. If such RTA-treated wafers are subjected to a further short anneal [7], the flat portion goes down, but the near-surface depleted regions remain narrow (curves 2 and 3 in Fig. 2, for an additional anneal at 975 °C for 18 and 58 s, respectively). Such a behaviour shows that the diffusivity of the monitored vacancy species is extremely low at 975 °C, not more than $10^{-7} \text{ cm}^2/\text{s}$ (this limit is indicated by the downward arrow in Fig. 1). In the bulk, the vacancy species are lost by some reaction not related to out-diffusion of these species. The curves 2 and 3 in Fig. 2 are reproduced assuming irreversible loss of vacancies at a rate $C_V(z)/\tau$. The loss time τ is specified [7] by the expression

$$1/\tau = (8 \times 10^{13} \text{ s}^{-1}) \exp(-3.88 \text{ eV}/kT). \quad (1)$$

This is close to 56 s at 975 °C. A most likely interpretation of these results [7] is that RTA freezes-in vacancy species of an extremely low diffusivity ($\leq 10^{-7} \text{ cm}^2/\text{s}$ at 975 °C), and these species (denoted V_s) are lost by conversion into another vacancy species which is dominant at this T . The most likely candidate for this species is the “Watkins vacancy” V_w that was observed in radiation experiments at cryogenic temperatures [3, 4].

The diffusivity D_w and the equilibrium concentration C_{w_e} of V_w play a key role in the subsequent analysis. The diffusivity [4] (solid line in Fig. 1) is

$$D_w = (0.0012 \text{ cm}^2/\text{s}) \exp(-0.45 \text{ eV}/kT). \quad (2)$$

The V_w species is likely [4, 6] to be responsible for a low- T branch in silicon self-diffusivity [11, 12] which gives a value of the $D_w C_{w_e}$ product. With the known D_w by Eq. (2), the equilibrium concentration C_{w_e} is specified as

$$C_{w_e} = (2 \times 10^{23} \text{ cm}^{-3}) \exp(-3.15 \text{ eV}/kT). \quad (3)$$

A normal pre-factor in this equation, on the order of the lattice site density, implies that V_w has a localized structure.

Extrapolated by Eq. (1) to $T_{\text{RTA}} = 1260 \text{ °C}$, the conversion time τ is 0.07 s, very short even on the time scale of fast cooling (several seconds). Therefore, the V_s and V_w species coexist, at T_{RTA} and in some interval below T_{RTA} , in the equilibrium ratio and accordingly diffuse as one entity with an averaged diffusivity

$$D_a = (D_w C_{w_e} + D_s C_{s_e}) / (C_{w_e} + C_{s_e}), \quad (4)$$

where the diffusivity–concentration product for the slow vacancy, $D_s C_{s_e}$, can be neglected. The value of D_a controls the width of vacancy-depleted zone in Fig. 2, and the estimate for the vacancy diffusivity at T_{RTA} , $10^{-5} \text{ cm}^2/\text{s}$, refers to D_a . This value is smaller than $D_w = 4 \times 10^{-5} \text{ cm}^2/\text{s}$ which means, by Eq. (4), that C_{w_e} (which is $9 \times 10^{12} \text{ cm}^{-3}$ at T_{RTA}) is essentially smaller than C_{s_e} .

On the other hand, C_{se} at T_{RTA} is somewhat larger than the Pt-measured concentration of $1.2 \times 10^{13} \text{ cm}^{-3}$ (Fig. 2) as some fraction of initial V_s may be lost even during fast cooling. Therefore, the requirement $C_{se} > C_{we}$ can be satisfied.

At lower T such as 975°C , a loss of V_s by conversion into V_w implies that the V_s species is now of a lower equilibrium concentration. This condition can be fulfilled only if the C_{se}/C_{we} ratio decreases rapidly upon lowering T which means that the formation energy E_s of V_s is well larger than $E_w = 3.15 \text{ eV}$ for V_w . The value of E_s will be fitted below to be about 4.9 eV . With this large number, both conditions, $C_{se} > C_{we}$ at T_{RTA} , and $C_{se} < C_{we}$ at 975°C , are satisfied.

3 Depth profiles of oxide precipitates in RTA-treated wafers The depth profiles of oxide precipitates, controlled by the RTA-installed vacancy profiles, are normally produced by a two-step anneal, $800^\circ\text{C}/4 \text{ h} + 1000^\circ\text{C}/16 \text{ h}$ that follows the RTA step. Profiles of a good resolution, and for various cooling rates, have been reported in reference. [13]; these are shown in Fig. 3. A remarkable feature of these profiles is that there is a wide almost flat middle portion (with some slight depression in the centre) surrounded by narrow near-surface zones of reduced precipitation (which correspond to the near-surface vacancy depletion by out-diffusion in Fig. 2). Upon reducing the cooling rate, and thus allowing a longer time for vacancy out-diffusion, the flat portion goes down but the near-surface depleted zones remain narrow (Fig. 3). This is just the same effect that was discussed in the previous section for Pt-monitored vacancy profiles. These data support the previous

conclusion that, in the course of cooling, the vacancy species out-diffuse only to a narrow depth. At the same time they are lost in the wafer bulk, and the loss mechanism is most likely the same as that discussed in the previous section, by a reconstruction of V_s into V_w . As was pointed out above, the V_s and V_w species are equilibrated close to T_{RTA} . A reversible exchange between V_s and V_w maintains the C_s/C_w ratio at the equilibrium value C_{se}/C_{we} . This ratio has been concluded to decrease quickly upon lowering T . Accordingly, a gradual redistribution between V_s and V_w , in favour of V_w , occurs in the course of cooling. The conversion time τ (T) increases, and soon becomes too long for a further redistribution to occur. The current concentration C_s of V_s is then frozen-in.

The model describing the evolution of the two related vacancy profiles in the course of cooling will be now discussed in more detail.

4 The model Each of the two concentration profiles, $C_s(z, t)$ for V_s and $C_w(z, t)$ for V_w , changes with time by the diffusion equation, with equilibrium boundary conditions at the sample surface. The diffusion of V_s can be neglected, due to very low diffusivity D_s . The diffusivity D_w is specified by Eq. (2). In addition, there is an exchange between the two vacancy species by the conversion reaction

$$dC_s/dt = -dC_w/dt = -(C_s - R_{sw}C_w)/\tau, \quad (5)$$

where $R_{sw} = C_{se}/C_{we}$ is the equilibrium concentration ratio of the two vacancy species. The conversion time τ is expressed by Eq. (1).

Even a short anneal (several seconds) is known [9, 10] to install an almost uniform vacancy profile. But the averaged diffusivity $D_a \approx 10^{-5} \text{ cm}^2/\text{s}$ of the $V_s + V_w$ community is too low for that. Therefore, this community should interact with an intrinsic point defect of a much higher diffusivity. There are two such defects: a silicon self-interstitial (denoted I), and a fast vacancy (V_f) that is responsible [5, 14, 15] for an appreciable vacancy contribution into self-diffusion at high T . The precise values of the parameters at T_{RTA} , the diffusivity D_I and the equilibrium concentration C_{Ie} for I, and the similar parameters D_f and C_{fe} for V_f , play a minor role in the simulations. We accept $D_I = 2 \times 10^{-4} \text{ cm}^2/\text{s}$ and $C_{Ie} = 3 \times 10^{13} \text{ cm}^{-3}$, close to those deduced in reference [5] and consistent with a well-known $D_I C_{Ie}$ product [16, 17]. The $D_f C_{fe}$ product is known [5, 14, 15] with a significant uncertainty. We will use the concentration C_{fe} as a fitting parameter; the diffusivity D_f does not affect the computed profiles, and it was tentatively adopted to be $10^{-4} \text{ cm}^2/\text{s}$.

As the $V_s + V_w$ community is equilibrated at T_{RTA} and below, it is not important which of the two species— V_s or V_w , or both—can recombine with I. Therefore only one recombination reaction can be considered, and it can be chosen to be $V_s + I$:

$$dC_s/dt = dC_I/dt = -\alpha_s(C_s C_I - C_{se} C_{Ie}). \quad (6)$$

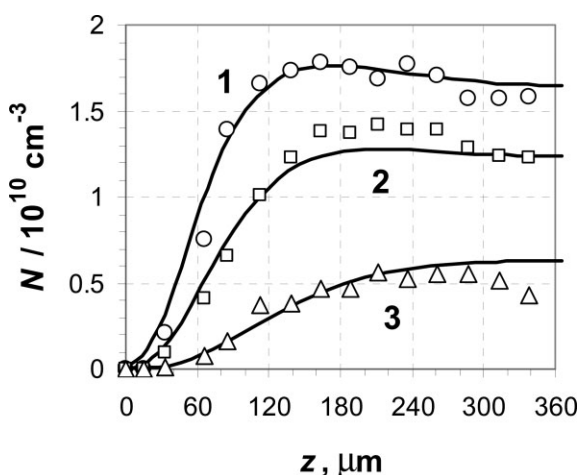


Figure 3 Depth profile of oxide precipitate density in RTA-treated wafers ($1280^\circ\text{C}/20 \text{ s}$ in Ar ambient) subjected to precipitation anneal sequence, $800^\circ\text{C}/4 \text{ h} + 1000^\circ\text{C}/16 \text{ h}$. The curves 1 (circles), 2 (squares), and 3 (triangles) correspond to the cooling rate of 70, 50, and 25 K/s , respectively. The experimental points (after Ref. [13]) are shown for the left half of the depth profile but the numbers are averaged over the two halves. The solid curves are simulated with the best-fit parameters specified in the text.

The kinetic recombination coefficient α_s is another fitting parameter.

The recombination of I with V_f is considered to be very fast-maintaining the $C_I C_f$ product at the equilibrium value $C_{Ie} C_{fe}$. The best fit is found assuming that C_{fe} is smaller than C_{Ie} ; in this case the V_f vacancies are completely annihilated by I, and the remaining point defects are self-interstitials and $V_s + V_w$. The self-interstitials disappear by out-diffusion and by a slow recombination with V_s , while the vacancy defects V_s and V_w are frozen-in.

The simulated dynamic system is simple: it is reduced to diffusion of all the species accompanied by two interaction reactions, Eq. (5) and (6). The simulated frozen-in profile $C_s(z)$ is sensitive mostly to assumed equilibrium concentration $C_{se}(T)$ of V_s specified by the value of C_{se} at T_{RTA} and by the formation energy E_s . The two other fitting parameters, C_{fe} and α_s , play a minor role.

5 Simulation results In performing the RTA treatment, the temperature is quickly ramped up to T_{RTA} , and the wafer is held at T_{RTA} for some time, typically 10 to 20 s. Then the wafer is rapidly cooled, this is the main step to establish the final depth profiles of the point defects. We have simulated the whole anneal sequence: ramp-up, holding at T_{RTA} for 20 s, cooling. We should bear in mind that the reported (nominal) value of T_{RTA} (which is 1280 °C for Fig. 3) may somewhat differ from the true temperature. In other studies [9, 10], similar precipitate densities were found for a lower nominal temperature, about 1240 °C, which means that the true temperatures were almost the same in both cases. For this reason we accept for simulations a compromise value of 1260 °C for T_{RTA} . The installed vacancy profile 1 (Fig. 2, for a nominal temperature of 1240 °C) is thus attributed to the same true temperature, 1260 °C.

The vacancy species which controls oxygen precipitation is identical to the Pt-monitored species V_s as the precipitation has been shown [10] to correlate with the installed vacancy concentration measured by Pt diffusion. The installed vacancy profile $C_V(z)$ relevant to nucleation of oxide precipitates is then $C_s(z)$. It is translated into the precipitate density profile by the presumed cubic dependence of N on the vacancy concentration:

$$N(z)/10^{10} \text{ cm}^{-3} = A [C_s(z)/10^{13} \text{ cm}^{-3}]^3. \quad (7)$$

The calibration coefficient A is selected to minimize the average deviation of the 3 computed $N(z)$ profiles (for 3 cooling rates) from the 3 experimental profiles of Fig. 3.

The procedure was to try different values of less relevant fitting parameters, C_{fe} and α_s , and for each combination to select the two major parameters C_{se} and E_s to minimize a deviation of the computed density profiles from the measured profiles of Fig. 3. An additional constraint is to minimize the deviation of computed $C_s(z)$, for the fastest cooling rate of 70 K/s, from the Pt-measured profile 1 of Fig. 2. A good fit can be achieved for $\alpha_s = 5 \times 10^{-15}$ to

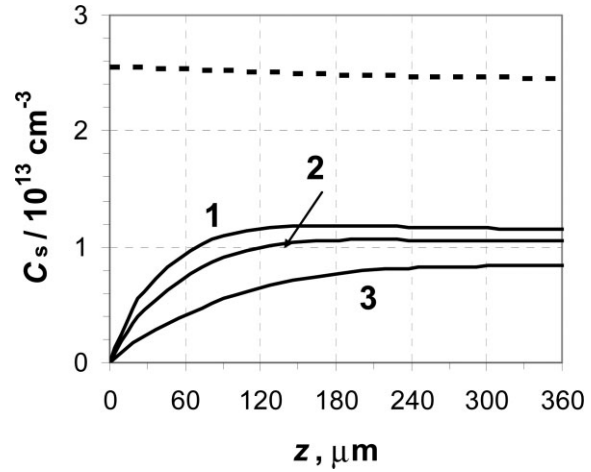


Figure 4 Simulated depth profiles of slow vacancy concentration C_s . The curves 1, 2, and 3 correspond to the cooling rate of 70, 50, and 25 K/s, respectively. The broken curve is the profile after holding at T_{RTA} for 20 s, prior to cooling.

$1.5 \times 10^{-14} \text{ cm}^3/\text{s}$ and for $C_{fe} = 10^{13}$ to $3 \times 10^{13} \text{ cm}^{-3}$. Within these ranges, the best-fit values of C_{se} and E_s are almost the same: C_{se} is close to $2.5 \times 10^{13} \text{ cm}^{-3}$ and E_s is close to 4.9 eV.

An example of the computed final vacancy profiles $C_s(z)$ is shown in Fig. 4 for three cooling rates: 70, 50, and 25 K/s (solid curves). The profile created by holding at T_{RTA} , and serving as a starting profile for subsequent relaxation during cooling, is shown by the broken curve. This profile is almost uniform (it would be uniform for longer holding time). The computed vacancy profile for the fastest cooling (curve 1 of Fig. 4) is close to the installed Pt-measured profile (curve 1 in Fig. 2).

To illustrate a redistribution between V_s and V_w in the course of cooling stage, the dependence of both concentrations on the temperature is shown in Fig. 5. Initially the concentration ratio C_s/C_w decreases following a reduction in the equilibrium ratio C_{se}/C_{we} . At lower T the redistribution is no longer efficient, due to an increased conversion time τ . The total vacancy concentration $C_s + C_w$ is slightly decreasing due to recombination with self-interstitials.

The density profiles corresponding to the vacancy profiles of Fig. 4 are shown by solid lines in Fig. 3; they provide a reasonably good fit to the measured profiles considering some remarkable scatter of the data. The calibration coefficient A in Eq. (7) is found to be 1.07.

6 Discussion and summary By previous analysis [6, 7] of the published data, and by the present more detailed consideration of the RTA-installed vacancy profiles, it appears that the shape of the profiles, in dependence of the cooling rate, is controlled by an exchange between two vacancy species: a slow vacancy V_s and a Watkins vacancy V_w . Both species are produced by RTA, but only one of them, a slow vacancy V_s , seems to be an “active” one: only

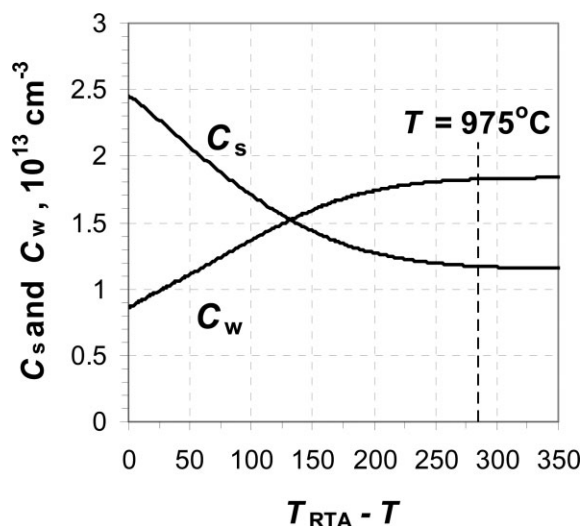


Figure 5 The concentrations of the V_s and V_w vacancy species in the course of lowering T from T_{RTA} , for $-dT/dt = 70$ K/s.

this species is measured by Pt diffusion, and only this species controls the nucleation of oxide precipitates (and thus the precipitate depth profiles). The properties of V_w are known, specified by the Eq. (2) and (3). For the diffusivity D_s of V_s only an upper limit (10^{-7} cm²/s at 975 °C) is known. Assuming for D_s an Arrhenius temperature dependence and a representative prefactor of 0.01 cm²/s, and identifying the diffusivity by Bracht in Fig. 1 with D_s , the migration energy of V_s can be estimated as 1.35 eV. The equilibrium concentration C_{se} has been deduced in the present study as

$$C_{se} = (3.1 \times 10^{29} \text{ cm}^{-3}) \exp(-4.9 \text{ eV}/kT). \quad (8)$$

A very large prefactor in this equation implies an extended nature of V_s .

The temperature dependence of the two equilibrium concentrations, $C_{we}(T)$ and $C_{se}(T)$ is illustrated in Fig. 6.

At T_{RTA} , the V_s and V_w species coexist in equilibrium, with the V_s species being the dominant one: $C_{se}/C_{we} \approx 2.8$. Upon cooling, these two species out-diffuse as one entity with an averaged diffusivity close to 10^{-5} cm²/s. It is essentially smaller than D_w since the mobile vacancy V_w is only a small part of the community. Upon lowering T , the C_{se}/C_{we} ratio decreases quickly, and a gradual redistribution in favour of V_w occurs. The frozen-in concentration of V_s is therefore well below the initial concentration at T_{RTA} . A reduction in C_s is more pronounced at a lower cooling rate. If a wafer is then annealed at low T like 975 °C, the redistribution from V_s to V_w goes on, as C_{se}/C_{we} is now small (≈ 0.14). This redistribution is further promoted considering that the V_w species is equilibrated [7] with the vacancy-oxygen complexes VO and VO₂, and the equilibrium concentration for the whole sub-community of $V_w + VO + VO_2$ may be still essentially larger than C_{we} .

Each of the two species V_s and V_w has a low diffusivity-concentration product, and accordingly gives only a small

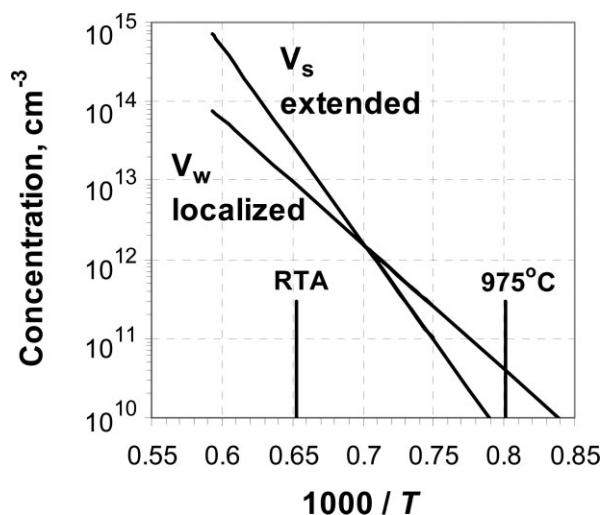


Figure 6 Equilibrium concentrations of two vacancy species, V_w and V_s . The left end of the curves corresponds to the melting point.

contribution into the self-diffusion coefficient at high T . However the vacancy contribution into high T self-diffusion is known [5, 14, 15] to be comparable to that by self-interstitials. This feature unambiguously shows that there is one more vacancy kind beside V_w and V_s : a fast vacancy V_f .

It raises an important question: what are the vacancy species responsible for void formation, at around 1100 °C?

The $V_w + V_s$ sub-community is definitely equilibrated as the cooling, for crystal growth, is much slower in comparison to RTA. The averaged diffusivity, by Eq. (4), is $D_a = 1.7 \times 10^{-5}$ cm²/s at 1100 °C. It is marginally consistent with a value resulting from void properties, so that the voids may be formed only by $V_w + V_s$, if this sub-community of vacancies does not exchange with V_f .

An alternative possibility is that all the three vacancy species, $V_s + V_w + V_f$, are equilibrated during crystal growth. The effective diffusivity, neglecting D_s , is

$$D_{eff} = (D_f C_{fe} + D_w C_{we}) / (C_{fe} + C_{we} + C_{se}). \quad (9)$$

The $D_f C_{fe}$ product is about 5×10^7 cm⁻¹s⁻¹ at 1100 °C [5], well larger than $D_w C_{we} = 1.4 \times 10^7$ cm⁻¹s⁻¹. Without a contribution of C_{fe} in the denominator of Eq. (9), D_{eff} would be too large, 7.5×10^{-5} cm²/s. To get a proper value for D_{eff} , about 3×10^{-5} cm²/s, the equilibrium concentration C_{fe} should be about 1.5×10^{12} cm⁻³, and the corresponding diffusivity D_f is then roughly 3.5×10^{-5} cm²/s.

If V_f is not equilibrated with $V_s + V_w$ during crystal growth, two different populations of voids may originate from these two vacancy sub-communities.

We can now give a simple explanation of the diffusivity data in Fig. 1. The RTA-based diffusivity (the bar confined by the squares) and the void-based diffusivity (the bar confined by the rhombic symbols) may be the two points of the same function $D_a(T)$ specified by Eq. (4). This (averaged)

diffusivity increases upon lowering T due to an increasing fraction of the fast species V_w within the $V_s + V_w$ community. The other diffusivity values, shown by the downward arrow and by the filled circles, refer to V_s ; in this range of lower T an exchange between V_s and V_w is slow.

Another important quantity, relevant to the point defect incorporation during crystal growth, is the melting point vacancy concentration. The concentration of V_w is expressed by Eq. (3) to be $C_{we} \approx 8 \times 10^{13} \text{ cm}^{-3}$, the concentration of V_s is now defined, by Eq. (8), to be $C_{se} \approx 7 \times 10^{14} \text{ cm}^{-3}$, but we cannot definitely specify C_{fe} . As the total vacancy concentration is unlikely to exceed 10^{15} cm^{-3} , the value of C_{fe} is expected to be not more than $3 \times 10^{14} \text{ cm}^{-3}$. The incorporated vacancies of all three kinds (V_s , V_w , and V_f) are likely to co-exist in the equilibrium ratio. Otherwise the vacancy aggregation into voids will be a more complicated phenomenon that it was thought previously.

In conclusion, the data on RTA-induced depth profiles of vacancies and of vacancy-based oxide precipitates can be well explained by considering two kinds of vacancies, a slow vacancy V_s and a Watkins vacancy V_w . These two vacancy species behave as one entity at higher T , but become independent one of the other at lower T . The total vacancy community in Si includes at least one more vacancy species, a fast vacancy V_f . An exchange between V_f and $V_s + V_w$ is believed to be negligible in RTA case, but it may be essential during crystal growth.

The V_w vacancy has a localized structure. The V_s and V_f species have an extended structure as evidenced by a large prefactor in C_{se} and in $D_f C_{fe}$, respectively. A possible atomic configuration of extended species may be a “morph” [18], a pocket of amorphous material within a crystalline matrix.

In the present analysis, a possible formation of di-vacancies has been neglected. Simple estimates [7] show that under the discussed experimental conditions, the di-vacancy concentration is negligible.

There is an “empty space” in the vacancy family of V_s , V_w , and V_f : is there also a slow localized vacancy species? If such a species does exist it may account for an ultrasonic elastic softening [19, 20] found in vacancy-populated crystal regions (but not in self-interstitial regions).

References

- [1] P. Pichler, *Intrinsic Point Defects, Impurities, and Their Diffusion in Silicon* (Springer, Wien, New York, 2004).
- [2] J. W. Corbett, G. D. Watkins, and K. S. McDonald, *Phys. Rev.* **135**, A1381 (1964).
- [3] G. D. Watkins, *Mater. Sci. Semicond. Process.* **3**, 227 (2000).
- [4] G. D. Watkins, *J. Appl. Phys.* **103**, 106106 (2008).
- [5] V. V. Voronkov and R. Falster, *Mater. Sci. Eng. B* **134**, 227 (2006).
- [6] V. V. Voronkov and R. Falster, *Solid State Phenom.* **205–206**, 157 (2014).
- [7] V. V. Voronkov, R. Falster, and P. Pichler, *Appl. Phys. Lett.* **104**, 032106 (2014).
- [8] H. Bracht, J. Fage Peterson, N. Zangenberg, A. Nylandsted Larsen, E. E. Haller, G. Lully, and M. Posselt, *Phys. Rev. Lett.* **91**, 245502 (2003).
- [9] M. Jacob, P. Pichler, H. Ryssel, R. Falster, M. Cornara, D. Gambaro, M. Olmo, and M. Pagani, *Solid State Phenom.* **57–58**, 349 (1997).
- [10] R. Falster, V. V. Voronkov, and F. Quast, *Phys. Status Solidi B* **222**, 219 (2000).
- [11] Y. Shimizu, M. Uematsu, and K. M. Itoh, *Phys. Rev. Lett.* **98**, 095901 (2007).
- [12] H. Bracht, R. Kube, E. Huger, and H. Schmidt, *Solid State Phenom.* **205–206**, 151 (2014).
- [13] M. Akatsuka, M. Okui, and K. Sueoka, *Nucl. Instrum. Methods Phys. Res. B* **186**, 45 (2002).
- [14] H. Bracht, E. E. Haller, and R. Clark-Felps, *Phys. Rev. Lett.* **81**, 393 (1998).
- [15] A. Ural, P. B. Griffin, and J. D. Plummer, *Phys. Rev. Lett.* **83**, 3454 (1999).
- [16] N. A. Stolwijk, B. Schuster, and J. Holzl, *Appl. Phys. A* **33**, 133 (1984).
- [17] H. Bracht, N. A. Stolwijk, and H. Mehrer, *Phys. Rev. B* **52**, 16542 (1995).
- [18] N. E. B. Cowern, S. Simdyankin, C. Ahn, N. S. Bennett, J. P. Goss, J.-M. Hartmann, A. Pakfar, S. Hamm, J. Valentin, E. Napolitani, D. De Salvador, E. Bruno, and S. Mirabella, *Phys. Rev. Lett.* **110**, 155501 (2013).
- [19] H. Yamada-Kaneta, T. Goto, Y. Nemoto, K. Sato, M. Hikin, Y. Saito, and S. Nakamura, *Solid State Phenom.* **131–133**, 455 (2008).
- [20] T. Goto, H. Yamada-Kaneta, Y. Saito, Y. Nemoto, K. Sato, K. Kakimoto, and S. Nakamura, *ECS Trans.* **3**, 375 (2006).